



Environment dependence of the growth of the most massive objects in the Universe

Krzysztof Bolejko, Jan J. Ostrowski

► To cite this version:

Krzysztof Bolejko, Jan J. Ostrowski. Environment dependence of the growth of the most massive objects in the Universe. *Physical Review D*, 2019, 99 (12), pp.124036. 10.1103/PhysRevD.99.124036 . hal-01815162

HAL Id: hal-01815162

<https://hal.science/hal-01815162>

Submitted on 5 Jul 2023

HAL is a multi-disciplinary open access archive for the deposit and dissemination of scientific research documents, whether they are published or not. The documents may come from teaching and research institutions in France or abroad, or from public or private research centers.

L'archive ouverte pluridisciplinaire **HAL**, est destinée au dépôt et à la diffusion de documents scientifiques de niveau recherche, publiés ou non, émanant des établissements d'enseignement et de recherche français ou étrangers, des laboratoires publics ou privés.

Spectral Adjustment Model's Analysis and Application to Remote Sensing Data

Jose Luis Villaescusa-Nadal , Belen Franch , Jean-Claude Roger , Eric F. Vermote, , and Chris Justice

Abstract—Differences in the relative spectral response functions of sensors lead to data inconsistencies that should be harmonized before multisensor exploitation. In this paper, we use spectral libraries to simulate satellite data and build models to correct them. We then explore and compare different models for coarse and medium spatial resolution optical sensors, including moderate resolution imaging spectroradiometer, advanced very high resolution radiometer (AVHRR), visible infrared imaging radiometer suite, multispectral instrument aboard Sentinel-2, and Operational Land Imager aboard Landsat 8. We found that optimal correction of different bands depends on the model used. For the green and near infrared bands, a multilinear land cover dependent regression improves the accuracy by up to 80.9%. For the red band, a novel exponential dependence of the spectral band adjustment factor with the normalized difference vegetation index (NDVI) provides an accuracy improvement of up to 72.8%. The best way to correct the NDVI value is to use the corrected NIR and red bands using these models. We apply the proposed methods to 445 BELMANIP2 sites using AVHRR data from the long-term data record from 1982–2017. High NDVI pixels result in 30-year trends varying up to 0.06 when comparing uncorrected to spectrally adjusted NDVI. Further application of these methods to NASA's Harmonized Landsat and Sentinel 2 product shows that for the red band and NDVI, our proposed method provides improved accuracy (54.6% and 62.5%) over the linear spectral adjustment currently used.

Index Terms—Advanced very high resolution radiometer (AVHRR), calibration, Landsat, moderate resolution imaging spectroradiometer (MODIS), normalized difference vegetation index (NDVI), relative spectral response, spectral band adjustment factor (SBAF), Sentinel 2, spectral adjustment, surface reflectance, visible infrared imaging radiometer suite (VIIRS).

I. INTRODUCTION

TO GAIN an understanding of land surface processes at a variety of scales, it is increasingly necessary to use data

from multiple Earth observation sensors [1]. By combining similar spatial resolution sensors, we can achieve higher temporal resolutions, increasing our ability to monitor rapidly changing phenomena and increase the opportunity of obtaining cloud-free observations. Additionally, the intercomparison between different sensors of basic parameters such as the surface reflectance is critical to build consistent databases. However, similar bands from different sensors have different spectral ranges and have a different band efficiency (or relative spectral response). This leads to a significant offset in the values measured, even when observing the same target at the same time [2]. Studies have shown differences in the normalized difference vegetation index (NDVI) value due to solely the relative spectral response (RSR). They can result in discrepancies of 6.3% between QuickBird and SPOT5 [3] that cause differences in the red and NIR reflectances of 20% and 4%, respectively [4]. It is, therefore, important to place all these sensors on a common radiometric scale, when generating a time series of a certain physical parameter covering different sensor generations and sensor types.

One way to achieve a common radiometric scale is to use an already well-calibrated sensor to calibrate other sensors (i.e., cross calibration) [5]. Cross calibration is a key toward the mission continuity, interoperability, and data fusion [1], [6], and is critical, when the sensor has no onboard reference available or when the vicarious calibrations are limited. This is the case for the advanced very high resolution radiometer (AVHRR) sensors, which started acquiring data in the 1980s. The AVHRR mission provides an unique dataset of 30+ years of global imagery, with daily temporal resolution. However, the time series consists of data from three different sensors onboard 13 different satellites. The RSR function of these sensors differ significantly, resulting in relative differences of around 15% in the red band, 3% in the NIR band, and 6% in the NDVI value, when comparing, for example, NOAA9 with NOAA15 [4]. These differences could result in problems when estimating parameters derived from the whole time-series, as they could produce inconsistencies between the sensors and misleading trends in the data, as will be shown in this study.

Regarding moderate to high spatial resolution, the Landsat series has been providing 16-day imagery since the 1970s. Due to such low temporal resolution of individual moderate spatial resolution satellites, there is a benefit in combining measurements from similar or analogous sensors aboard different satellites [7]. With the launch of Sentinel 2 [8], the combination of Landsat 8 and Sentinel 2 data provides a significant improvement

Manuscript received September 12, 2018; revised November 6, 2018; accepted December 4, 2018. Date of publication January 7, 2019; date of current version March 25, 2019. This work was supported by the NASA grant "Support for the HLS (Harmonized Landsat-Sentinel-2) Project" (NNX16AN88G). (Corresponding author: Jose Luis Villaescusa-Nadal.)

J. L. Villaescusa-Nadal, B. Franch, J.-C. Roger, and S. Skakun are with the Department of Geographical Sciences, University of Maryland, College Park, MD 20742 USA, and NASA Goddard Space Flight Center, Greenbelt, MD 20771 USA (e-mail: jvillaes@umd.edu; befranch@umd.edu; roger63@umd.edu; skakun@umd.edu).

E. F. Vermote is with the NASA Goddard Space Flight Center, Greenbelt, MD 20771 USA (e-mail: Eric.F.Vermote@nasa.gov).

C. Justice is with the Department of Geographical Sciences, University of Maryland, College Park, MD 20742 USA (e-mail: cjustice@umd.edu).

Color versions of one or more of the figures in this paper are available online at <http://ieeexplore.ieee.org>.

Digital Object Identifier 10.1109/JSTARS.2018.2890068

in temporal resolution [9]. The Harmonized Landsat/Sentinel-2 (HLS) Project, for example, provides a surface reflectance product combining both satellite's measurements at 30-m spatial resolution [10]. In this case, it is important to consider the directional and atmospheric effects resulting from the difference in overpass time and observation angle of each satellite, along with the spectral correction [7].

The purpose of radiometric adjustment is to correct differences due to discrepancies in the RSR function between analogous bands. These differences can only be compared when the spectral responses of the sensors for a given band have enough spectral overlap [11]. Several different ways to correct spectral differences have been reported in the literature and can be generally classified into three main types: band averaging, radiative transfer, and statistical regression. The latter is the most commonly used in the literature and consists in using hyperspectral data convolutions [12], [13], remotely sensed observations [14], [15], or radiative transfer calculation [16] to obtain regression coefficients that establish a relationship between analogous bands.

The most commonly used relationship is the linear regression [13], [16]. It involves using a simple relationship between the reference (ref) and target (tar) sensors to obtain correction parameters which can later be used to correct any target sensor's observation. This method is used in the HLS product [17], using Landsat-8 as a reference. The main reason behind its popularity is its simplicity and practical use, however it overestimates low NDVI values and underestimates high NDVI values, suggesting that its optimal use is for intermediate NDVI values [18]. Previous studies have shown that the reflectance relationships between the red and NIR bands have strong land cover dependencies [19], which are not considered when using the linear regression. They can, however, be corrected as a function of the quadratic NDVI [4], [19], [20]. Differences in the spectral band adjustment factor (SBAF), defined as the ratio between the target and reference reflectance, can increase up to 30% and 40% in the red and NIR bands, respectively [4]. Fan and Liu [11] determined that the SBAF between Landsat TM and Earth Observing One (EO-1) Advanced Land Imager (ALI) is inherently dependent on the NDVI and exhibit nonlinear dependencies. To correct discrepancies between similar NDVI values of soils and sparsely vegetated land cover for varying RSRs, D'Odorico *et al.* [21] added to the regression model the red and NIR bands, providing further information on the land cover type by means of a multilinear regression. The quadratic approach does not seem to fully correct these nonlinearity problems when the spectral differences are big, and the bands are wide for extreme NDVI values, so we propose an exponential correction function which models the saturation of high NDVI values for pixels with a high leaf area index (LAI) accurately.

These studies, however, do not hypothesize that different bands should be corrected using different models. The sensitivity analysis performed in [19] leads to our hypothesis that the land cover dependencies of bands which overlap with the green peak or red-edge regions in different ways, should be modeled differently. The aim of this paper is to test said hypothesis by comparing the performance of different spectral adjustment

TABLE I
PASSIVE OPTICAL SENSORS CONSIDERED AND THEIR OFFICIAL BAND NUMBER

Mission/s	Sensor	Green band	Red band	NIR band
NOAA8, 10	AVHRR/1	-	1	2
NOAA7, 9, 11, 12, 13, 14	AVHRR/2	-	1	2
NOAA15,16,17,18,19	AVHRR/3	-	1	2
Landsat 4, 5	TM	2	3	4
Landsat 7	ETM+	2	3	4
Landsat 8	OLI	3	4	5
Aqua/Terra	MODIS	4	1	2
Sentinel 2A/B	MSI	3	4	8A
Suomi NPP	VIIRS	-	11	12

methods on the green, red, NIR, and NDVI. We then apply the selected methods on real data to test their performance. We do this by comparing coincident Landsat 8 and Sentinel 2 images from the NASA's HLS product [10]. We finally analyze the impact of the spectral differences on time series trends by studying AVHRR data. Section II describes the materials used for the study. Section III presents the methodology. Section IV presents the results. Section V presents a discussion of the results and Section VI presents the conclusion.

II. MATERIALS

A. Sensors Used

Table I shows the optical sensors and spectral bands considered in this study. Same sensors on different missions have different spectral responses. The RSR functions were downloaded from <https://cloudsway2.larc.nasa.gov/> and are shown in Fig. 1.

1) *Moderate Resolution Imaging Spectroradiometer (MODIS)*: The MODIS is an instrument aboard the Terra and Aqua missions, which provides daily measurements at coarse spatial resolution (1 km–250 m). It acquires data in 36 spectral bands, with a very similar RSR for both satellites. It was designed to produce large-scale global measurements. MODIS is widely used in the remote sensing community due to the quality of its calibration [22], [23] and validation [24], [25], so we selected it as a reference sensor. The choice of Aqua over Terra is arbitrary given their almost identical RSR function. In this study, we only consider the red, NIR, and green bands, with band numbers 1, 2, and 4, respectively.

2) *Visible Infrared Imaging Radiometer Suite (VIIRS)*: The VIIRS is an instrument aboard the Suomi National Polar-orbiting Partnership (Suomi-NPP) satellite. It provides daily observations at coarse spatial resolution, similar to MODIS; its purpose is to continue the heritage of the NOAA AVHRR and MODIS products, enabling characterization of the land surface at regional to global scales. We use the I1 and I2 bands, due to the presence of analogous bands in the MODIS or AVHRR sensors.

3) *Landsat and Sentinel 2*: The Landsat program has been providing information about the Earth at moderate spatial resolution (70–30 m) since the 1970s, increasing our understanding

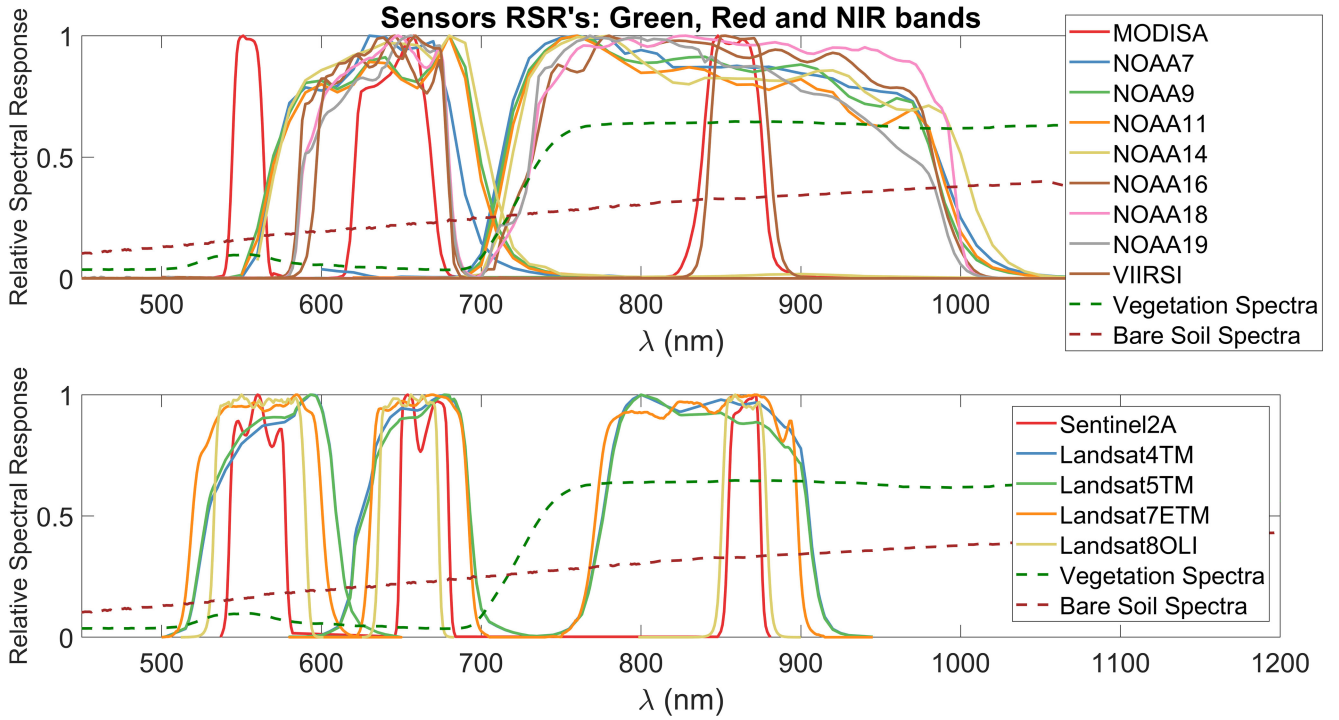


Fig. 1. RSR of the sensors used in this study for the green, red, and NIR bands specified in Table I. The dashed lines show a typical vegetation and bare soil spectra.

of local environmental changes. The most recent satellite, Landsat 8, was launched in 2013 and provides measurements every 16 days. The Sentinel 2A satellite, launched by ESA in 2015, has similar characteristics. The Harmonized Landsat/Sentinel2 product provides a combination of measurements approximately every five days, correcting for geometric, anisotropic, atmospheric, and spectral differences [10].

We downloaded HLS data for seven SURFRAD sites in the U.S. [26] and six sites in Australia (HLS tiles 54HVVH, 55HBU, 55HCV, 55HDB, 56HKH, and 56JMQ) where Landsat 8 and Sentinel 2 sensors have coincident observations (131 scenes). The data were corrected for geometric sampling and geographic registration, but in this study were not corrected for directional effects.

The Equator crossing times of the Landsat 8 OLI and Sentinel-2 MSI sensors are close, 10:00 A.M. (L8) and 10:30 A.M. (S2), and the viewing angles from nadir are $\pm 7.5^\circ$ and $\pm 10.3^\circ$, respectively [27]. This means that the illumination conditions for coincident dates are very similar, and the differences in surface reflectance due to the surface anisotropy can be considered negligible for low observation angles. The spectral differences between the L8 OLI and S2 MSI sensors are significant for the green and red bands, but negligible for the NIR bands (see Fig. 1), with band numbers specified in Table I. For these reasons, the use of this product for data on the same site and day allows a reasonable comparison between the two sensors whose difference can be attributed mainly to the spectral differences.

4) *Advanced Very High Resolution Radiometer*: The AVHRR surface reflectance data from 1982 to 2017 were obtained from the long-term data record (LTDR) surface

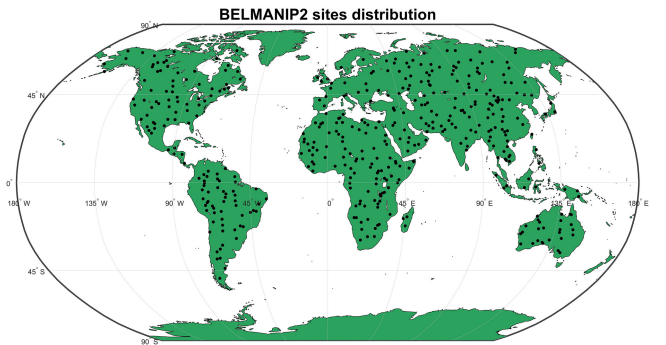


Fig. 2. Distribution of the BELMANIP2 (black dots) sites around the world.

reflectance database [28] produced by NASA's Goddard Space Flight Center and the University of Maryland. These daily data are mapped into a climate modeling grid at $0.05^\circ \times 0.05^\circ$ resolution, corresponding to a 3600×7200 pixel array over the globe. It is corrected for directional effects [29], [30], but not for spectral effects [28]. We downloaded AVHRR time series for 445 BELMANIP2 sites. BELMANIP2 sites are an update of BELMANIP1 [31] and were selected because they represent the variability of vegetation types and climatological conditions around the world. The spatial distribution of these sites is shown in Fig. 2.

B. Spectral Libraries

We considered 615 surface reflectance spectral profiles from ground measurements and atmospherically corrected airborne

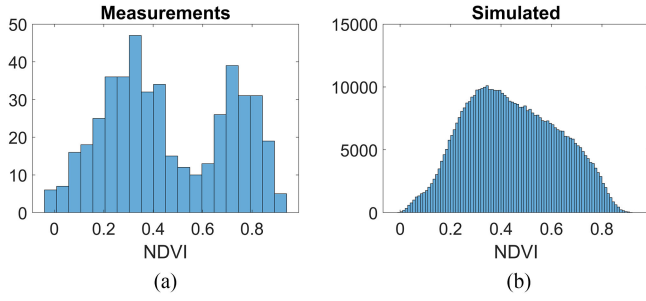


Fig. 3. NDVI distribution of the surface reflectance spectra used in this study. (a) Before mixing spectral reflectance values. (b) After mixing spectral reflectance values.

visible and infrared imaging spectrometer measurements [32] included in the USGS [33] spectral libraries. These profiles covered a wide range of land covers, including snow, ice, rocks, soils, vegetation, and manmade materials such as asphalt or brick. Overall, they were distributed along the NDVI range from 0 to 0.93 [see Fig. 3(a)].

III. METHODS

A. Algorithm Description

Field measurements are only representative of very specific types of surfaces. When working with coarse resolution data, the measured signal of a given pixel is most often a combination of signals from different surfaces (mixed pixels). Therefore, to make the field measurements more representative of the remotely sensed signal while also increasing the sample size, we simulated random combinations of these spectra. We did this by linearly combining the reflectance spectra of the 615 field measurements. Up to three different field measurements were combined each time to reproduce a coarse resolution remote sensing pixel. We assigned to each one of them a random weight, which represents the percentage cover of that land type in a certain pixel. The number of possible combinations using three different surfaces added up to ~ 16 million, but we selected a random sample of 500 000 spectra. The NDVI range of the original samples is shown in Fig. 3(a), while that of the combined satellite representative samples is shown in Fig. 3(b).

Having selected the reference hyperspectral data, we applied the spectral adjustment to simulate what the different sensors would measure if only the spectral differences between them were considered. We do this by weighing measured reflectances by their RSR and obtaining the simulated reflectances of each band

$$\bar{\rho}_\lambda = \frac{\int \rho_\lambda \text{RSR}_\lambda d\lambda}{\int \text{RSR}_\lambda d\lambda} \quad (1)$$

where ρ_λ is the spectral library's reflectance, the RSR is the RSR function of the sensor, and $\bar{\rho}_\lambda$ the simulated reflectance of the sensor. We calculated the ratio of simulated reflectances from two different sensors; a reference sensor $\bar{\rho}_{\lambda,\text{ref}}$ and a target

sensor $\bar{\rho}_{\lambda,\text{tar}}$, also known as the SBAF using

$$\text{SBAF} = \frac{\bar{\rho}_{\lambda,\text{ref}}}{\bar{\rho}_{\lambda,\text{tar}}} \quad (2)$$

We then proceeded to build the models described in detail in Section III-B and retrieve the corresponding regression coefficients, using MODIS/Aqua as a reference. These coefficients were applied to the surface reflectance data to allow the comparison of the different methods over different sensor combinations. This comparison is assessed in terms of the accuracy, precision, and uncertainty (APU) metrics [34]. The accuracy represents the mean bias of the estimates, against reference data. It is also known as the mean bias error. The precision represents the repeatability of the estimate, and it computes the standard deviation of the estimates around the reference values corrected for the bias (accuracy). Finally, the uncertainty, or root mean square error (RMSE), is the deviation of the estimate from the reference.

The surface reflectance bands analyzed are the green, red, and NIR, but we also compute the corrected NDVI. The two schemes generally used in the literature for NDVI correction are the distributed and lumped schemes. The former initially corrects the spectral bands and then calculates the NDVI from them (3), while the latter computes an intercalibration equation from the NDVI (NDVI-to-NDVI) [18], [35]

$$\text{NDVI}_{\text{corrected}} = \frac{\rho_{\text{NIR,corrected}} - \rho_{\text{red,corrected}}}{\rho_{\text{NIR,corrected}} + \rho_{\text{red,corrected}}} \quad (3)$$

In the case that our hypothesis is valid and different methods are used to correct different bands, we can calculate the NDVI using the distributed scheme through the NIR band corrected using one model, and the red band corrected using a different model.

B. Spectral Methods Description

The empirical regression models and SBAF methods that have been tested in this paper are the following.

1) Linear Model:

$$\bar{\rho}_{\lambda,\text{ref}} = a + b \cdot \bar{\rho}_{\lambda,\text{tar}} \quad (4)$$

2) *Multilinear Regression Model 1 (MRI)*: Strong land cover dependencies have been observed in the red and NIR bands' intercalibration, but none have been reported for the green band, so analogous to the red and NIR multilinear regression

$$\bar{\rho}_{(\text{red,nir}),\text{ref}} = \beta_1 \bar{\rho}_{\text{red,tar}} + \beta_2 \bar{\rho}_{\text{nir,tar}} + \beta_3 \text{NDVI} + \beta_4 \text{NDVI}^2 + \epsilon \quad (5)$$

We model the green band in the following way:

$$\bar{\rho}_{\text{green,ref}} = \beta_1 \bar{\rho}_{\text{green,tar}} + \beta_2 \bar{\rho}_{\text{nir,tar}} + \beta_3 \text{NDVI} + \beta_4 \text{NDVI}^2 + \epsilon \quad (6)$$

We avoided the inclusion of both green and red bands in the same model, given their high correlation ($R > 0.9$) to reduce the significant multicollinearity effects.

3) *Multilinear Regression Model 2 (MR2)*: To characterize the land cover dependencies without the use of the NDVI, which becomes saturated at high LAI values (dense vegetation canopies), we propose a second version of the multilinear regression model which considers products and second-order polynomials of the spectral bands

$$\begin{aligned} \bar{\rho}_{(g,red,nir),ref} = & \beta_1 \bar{\rho}_{(g,red),tar} + \beta_2 \bar{\rho}_{nir,tar} \\ & + \beta_3 (\bar{\rho}_{(g,red),tar} * \bar{\rho}_{nir,tar}) + \beta_4 (\bar{\rho}_{(g,red),tar})^2 \\ & + \beta_5 (\bar{\rho}_{nir,tar})^2 + \epsilon. \end{aligned} \quad (7)$$

To ensure that “black” surfaces have the same values for both target and reference sensors, both multilinear models are fit without a constant term.

4) *SBAF Quadratic NDVI*: Equation (8) shows the regression approach for the green, red, and NIR bands, using the SBAF

$$SBAF = \frac{\bar{\rho}_{\lambda,ref}}{\bar{\rho}_{\lambda,tar}} = a + b \cdot NDVI + c \cdot NDVI^2. \quad (8)$$

5) *SBAF Exponential NDVI*: An exponential fit is proposed (9), which is steeper in the high and gentler in the low NDVI values, to account for the NDVI saturation for high LAI values [36]

$$SBAF = \frac{\bar{\rho}_{\lambda,ref}}{\bar{\rho}_{\lambda,tar}} = a \cdot e^{b \cdot NDVI} + c \cdot e^{d \cdot NDVI}. \quad (9)$$

C. Propagation of Uncertainties

When these adjustment equations are used with real data to correct for spectral effects, uncertainties from the surface reflectance measurements are propagated to the corrected reflectance. This means that, even if we found theoretically that a certain model performed better in terms of uncertainty than another model, this might not be the case operationally. For this reason, we simulate surface reflectance data with a 5% uncertainty and analyze the propagated uncertainties for the different models considered. Equation (10) shows the propagated uncertainty (σ_f) of a function $f(x,y)$. (σ_x, σ_y) are the uncertainties of x and y , and $\sigma_{x,y}$ is the covariance between x and y

$$\sigma_f^2 = \left| \frac{\partial f}{\partial x} \right|^2 \sigma_x^2 + \left| \frac{\partial f}{\partial y} \right|^2 \sigma_y^2 + 2 \left(\frac{\partial f}{\partial x} \right) \left(\frac{\partial f}{\partial y} \right) \sigma_{x,y}. \quad (10)$$

D. HLS Product

To select low observation angles for Landsat 8, we use the image metadata and extract the images that compose a specific HLS image. We then identify the pixels from the tile with a close to nadir observation (viewing angle $< 2^\circ$) using the trajectory overpass and tile geolocation. We do the same with Sentinel 2 images and select those pixels which overlap for both sensors. Overall, we obtained 1.7×10^7 coincident pixels. From these, we masked pixels with high aerosol values to minimize atmospheric effects.

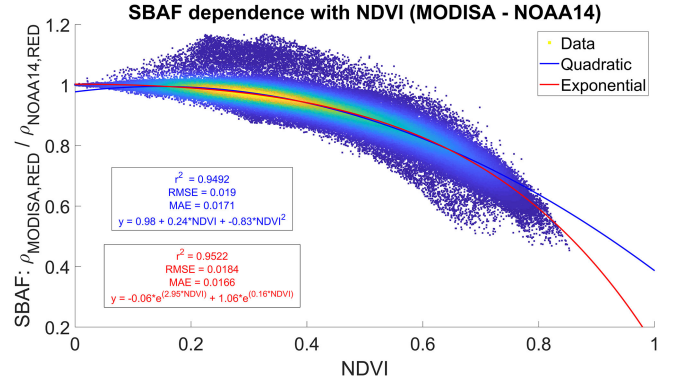


Fig. 4. SBAF dependence between MODIS Aqua (reference) and NOAA14 (target) based on the simulated data. The quadratic fit is shown in blue and the exponential fit in red.

E. AVHRR Time Series

In this section, we computed the NDVI value from the different sensor's surface reflectance which combines AVHRR/2 and AVHRR/3 measurements from the NOAA 7, 9, 11, 14, 16, and 18 satellites to produce a 36-year NDVI time series. We then corrected the time series using the different spectral adjustment parameters explained in detail in the following section and performed a Mann–Kendall correlation coefficient test [37], [38] to analyze the significance of the trends for each method. We used the Sen's slope method [39] to compute said trends and compared their value for the different methods proposed. The slope's confidence intervals were obtained by using the 95 and 5 percentiles of the individual slopes [40].

IV. RESULTS

A. Model Comparisons With Simulated Data

To justify the use of the SBAF exponential model as a correction to the SBAF quadratic model, Fig. 4 shows the SBAF dependence with the NDVI between simulated MODIS/Aqua data as a reference sensor and AVHRR/2 (NOAA14) as a target sensor. The blue line represents the quadratic fit, and the red line the exponential fit. The former shows some problems for low (< 0.2) and high (> 0.7) NDVI values, which are correctly modeled by the latter, evidenced by a decrease of RMSE and MAE of $\sim 3\%$.

Table II shows the absolute values ($\times 10^{-3}$) and percentage improvements in the APU values for the green, red, and NIR bands of four different sensors (L8, NOAA14, VIIRS, and S2) using the spectral adjustment regression methods considered in this paper. The retrieved coefficients for every sensor combination are available at <http://ltdri.org/salsa/>. MODIS/Aqua is used as the reference sensor. The improvements are calculated with respect to the spectrally uncorrected surface reflectance data, and the method that shows the highest increase for each case is highlighted. In the green band, the highest improvement in the accuracy is given by the SBAF exponential method, and the highest improvement in the precision and uncertainty is given by the MR1. In the case of S2, for example, the APU values increase

TABLE II
ACCURACY (A), PRECISION (P), AND UNCERTAINTY (U) VALUES AND % IMPROVEMENT OF THE SPECTRAL ADJUSTMENT REGRESSION METHODS CONSIDERED WITH RESPECT TO THE UNCORRECTED SIMULATED DATA

		Method	Target Sensor			
			L8 OLI	AVHRR/2 (NOAA14)	VIIRS	S2 MSI
GREEN	A	Uncorrected	3.44			2.45
		Linear	3.32 (3.49%)			2.13 (12.88%)
		Multilinear 1	2.27 (34.14%)			1.56 (36.32%)
		Multilinear 2	2.82 (18.07%)			1.89 (22.75%)
		SBAF Quadratic	2.12 (38.49%)			1.58 (35.38%)
		SBAF Exp	2.10 (38.93%)			1.55 (36.84%)
	P	Uncorrected	4.50			2.98
		Linear	4.36 (3.23%)			2.82 (5.33%)
		Multilinear 1	3.17 (29.63%)			2.18 (26.57%)
		Multilinear 2	4.02 (10.67%)			2.61 (12.27%)
		SBAF Quadratic	3.27 (27.28%)			2.46 (17.48%)
		SBAF Exp	3.26 (27.65%)			2.40 (19.24%)
	U	Uncorrected	4.50			3.31
		Linear	4.36 (3.65%)			2.82 (14.78%)
		Multilinear 1	3.17 (29.61%)			2.20 (33.46%)
		Multilinear 2	4.02 (10.46%)			2.63 (20.52%)
		SBAF Quadratic	3.27 (27.51%)			2.46 (25.55%)
		SBAF Exp	3.26 (27.89%)			2.41 (27.17%)
RED	A	Uncorrected	2.70	10.13	2.50	5.92
		Linear	2.31 (14.33%)	6.42 (36.57%)	0.9 (19.34%)	5.07 (14.4%)
		Multilinear 1	2.07 (23.48%)	2.85 (71.84%)	1.77 (29.38%)	4.53 (23.45%)
		Multilinear 2	2.02 (25.21%)	2.78 (72.55%)	1.73 (30.79%)	4.44 (24.94%)
		SBAF Quadratic	1.97 (26.92%)	2.84 (71.97%)	1.66 (33.57%)	4.37 (26.24%)
		SBAF Exp	1.97 (26.99%)	2.75 (72.82%)	1.67 (33.34%)	4.36 (26.37%)
	P	Uncorrected	3.70	8.71	3.47	8.33
		Linear	3.34 (9.63%)	8.29 (4.82%)	1.30 (11.27%)	7.53 (9.52%)
		Multilinear 1	3.21 (13.36%)	4.99 (42.73%)	2.96 (14.74%)	7.22 (13.27%)
		Multilinear 2	3.25 (12.05%)	4.96 (42.97%)	3.03 (12.64%)	7.29 (12.47%)
		SBAF Quadratic	3.14 (15.15%)	4.94 (43.31%)	2.83 (18.42%)	7.09 (14.86%)
		SBAF Exp	3.14 (15.17%)	4.86 (44.19%)	2.84 (18.29%)	7.09 (14.91%)
	U	Uncorrected	3.91	12.88	3.84	8.67
		Linear	3.34 (14.55%)	8.29 (35.65%)	1.30 (19.91%)	7.53 (13.1%)
		Multilinear 1	3.24 (17.31%)	5.00 (61.18%)	3.02 (21.34%)	7.25 (16.4%)
		Multilinear 2	3.30 (15.61%)	4.98 (61.34%)	3.12 (18.88%)	7.35 (15.2%)
		SBAF Quadratic	3.14 (19.72%)	4.94 (61.66%)	2.84 (26.05%)	7.09 (18.23%)
		SBAF Exp	3.14 (19.74%)	4.86 (62.27%)	2.85 (25.94%)	7.09 (18.27%)
NIR	A	Uncorrected	2.09	13.13	1.15	2.17
		Linear	0.87 (58.47%)	4.55 (65.34%)	0.52 (54.75%)	0.91 (57.76%)
		Multilinear 1	0.84 (59.79%)	2.56 (80.53%)	0.50 (56.67%)	0.89 (58.81%)
		Multilinear 2	0.85 (59.42%)	2.51 (80.85%)	0.51 (56.01%)	0.90 (58.55%)
		SBAF Quadratic	0.99 (52.56%)	2.71 (79.35%)	0.60 (48.17%)	1.05 (51.73%)
		SBAF Exp	0.98 (53.03%)	2.71 (79.33%)	0.59 (48.44%)	1.03 (52.30%)
	P	Uncorrected	1.18	7.87	0.70	1.26
		Linear	1.18 (0.35%)	5.95 (24.45%)	0.70 (0.00%)	1.25 (0.45%)
		Multilinear 1	1.15 (3.03%)	3.41 (56.71%)	0.68 (3.26%)	1.22 (2.66%)
		Multilinear 2	1.15 (2.60%)	3.38 (57.02%)	0.69 (2.40%)	1.23 (2.42%)
		SBAF Quadratic	1.30 (-9.58%)	3.58 (54.46%)	0.78 (-10.85%)	1.37 (-9.14%)
		SBAF Exp	1.29 (-9.11%)	3.59 (54.43%)	0.78 (-10.65%)	1.37 (-8.54%)
	U	Uncorrected	2.39	15.27	1.34	2.48
		Linear	1.18 (50.53%)	5.95 (61.07%)	0.7 (47.42%)	1.25 (49.59%)
		Multilinear 1	1.16 (51.56%)	3.41 (77.68%)	0.69 (48.77%)	1.23 (50.45%)
		Multilinear 2	1.16 (51.38%)	3.38 (77.85%)	0.69 (48.34%)	1.23 (50.37%)
		SBAF Quadratic	1.31 (45.26%)	3.59 (76.48%)	0.79 (41.36%)	1.38 (44.38%)
		SBAF Exp	1.30 (45.49%)	3.59 (76.46%)	0.78 (41.48%)	1.37 (44.68%)

The method with the best improvement for each target sensor is highlighted in green. Absolute values of A, P, and U are expressed in 10^{-3} reflectance for easier comparison.

up to 36.8%, 26.6%, and 33.5%, respectively. In the precision and the uncertainty, the difference between the two methods is around 7% and 6%, respectively. In the red band, the highest improvement in all three metrics is given by the SBAF exponential method. The improvements for the AVHRR/2 aboard NOAA14 are of 72.8% in the accuracy, 44.2% in the precision, and 62.3% in the uncertainty.

The values are similar to the SBAF quadratic correction method for most sensor combinations. The worst performance in every case is achieved using the linear method, which provides only a minor correction with respect to the spectrally uncorrected values. In the case of the green L8 band, for example, it only corrects 3.5% of the accuracy, as compared to the 38.9% provided by the SBAF exponential method.

TABLE III
ANALOGOUS TO TABLE II BUT FOR THE NDVI

			Target Sensor			
		Method	L8 OLI	AVHRR/2 (NOAA14)	VIIRS	S2 MSI
NDVI	A	Raw	5.66	41.01	6.83	13.33
		Linear	5.30 (6.35%)	20.92 (48.99%)	4.97 (27.30%)	11.94 (10.40%)
		Multilinear 1	4.50 (20.54%)	7.01 (82.90%)	4.29 (37.14%)	10.18 (23.67%)
		Multilinear 2	4.38 (22.61%)	6.70 (83.67%)	4.08 (40.21%)	9.97 (25.19%)
		SBAF Quadratic	4.28 (24.50%)	6.88 (83.22%)	4.01 (41.30%)	9.77 (26.70%)
		SBAF exp	4.28 (24.43%)	6.78 (83.47%)	4.01 (41.24%)	9.77 (26.69%)
		MR1-Exp	4.27 (24.69%)	6.67 (83.74%)	3.98 (41.70%)	9.77 (26.71%)
	P	Raw	7.57	25.39	7.51	17.96
		Linear	7.14 (5.79%)	25.51 (-0.48%)	6.56 (12.6%)	16.59 (7.64%)
		Multilinear 1	6.54 (13.61%)	10.36 (59.18%)	6.07 (19.07%)	15.24 (15.13%)
		Multilinear 2	6.53 (13.85%)	10.14 (60.05%)	6.00 (20.02%)	15.24 (15.15%)
		SBAF Quadratic	6.44 (15.04%)	10.17 (59.95%)	5.78 (22.98%)	15.03 (16.31%)
		SBAF exp	6.43 (15.05%)	10.08 (60.28%)	5.78 (22.97%)	15.03 (16.31%)
		MR1-Exp	6.43 (15.16%)	10.02 (60.53%)	5.78 (23.02%)	15.03 (16.32%)
	U	Raw	7.58	47.77	8.83	18.05
		Linear	7.14 (5.78%)	25.79 (46.01%)	6.56 (25.72%)	16.6 (8.07%)
		Multilinear 1	6.59 (13.04%)	10.38 (78.27%)	6.19 (29.92%)	15.30 (15.27%)
		Multilinear 2	6.58 (13.11%)	10.16 (78.73%)	6.16 (30.26%)	15.32 (15.13%)
		SBAF Quadratic	6.45 (14.88%)	10.17 (78.71%)	5.83 (34.01%)	15.04 (16.68%)
		SBAF exp	6.45 (14.89%)	10.08 (78.89%)	5.83 (34.00%)	15.04 (16.67%)
		MR1-Exp	6.44 (15.05%)	10.02 (79.02%)	5.83 (34.00%)	15.04 (16.71%)

Table III is analogous to Table II, but for the NDVI. In the NIR band, the MR1 approach provided the best improvements in APU for every sensor combination except for NOAA14, where the MR2 provided a slightly better improvement ($\sim 0.3\%$ better in the Accuracy and Precision, and $\sim 0.2\%$ better in the Uncertainty). The overall improvements in APU for NOAA-14 increase up to 80.9%, 57%, and 77.85%, respectively. For the NDVI value, we add an extra model, the MR1-Exp, to present what the optimum NDVI correction would be, that is, correcting the red and NIR bands with the model that performs best for each band and calculating the NDVI from them. The methods selected were the MR1 for the NIR band and the SBAF-Exp for the red band (MR1-Exp). The best improvement for the NDVI value in terms of the APU is provided by this approach, correcting the accuracy by 24.7%, 83.7%, 41.7% and 26.7% for L8, NOAA14, VIIRS, and S2 sensors, respectively.

B. Propagation of Uncertainties

Fig. 5 shows the propagated relative and absolute uncertainties (solid line-left axis and dashed line-right axis, respectively) for the adjustment functions used in this study, as a function of the NDVI. The red and blue lines represent the uncertainty for the red and NIR bands. There are different red-NIR combinations that would yield the same NDVI values, so every curve represents the average uncertainty of every NDVI value, hence the nonlinear shapes. The last graph compares the propagated relative and absolute uncertainty for the distributed (red) and lumped (blue) methods. The data were modeled using MODIS Aqua as a reference and Landsat 8 as a target sensor, as an example. These results show that the absolute values are almost identical between every method and band, but that the relative uncertainties vary up to $\sim 1\%$ for the red band and stay constant for the NIR band. Other sensor combinations with a higher NDVI dependency exhibited even higher differences in the

relative values. In the NDVI comparison, the absolute uncertainty of the distributed method is slightly lower than the lumped method, but the relative uncertainty is very similar, becoming very high for low NDVI values.

C. HLS Data

We calculated the average uncertainty for the Landsat8 and Sentinel2A sensors, obtaining a percentage difference of $\sim 1.5\%$, $\sim 3.0\%$, and 0.03% for the green, red, and NIR bands, respectively.

Fig. 6 shows the accuracy (orange), precision (green), and uncertainty (blue) comparison (right axis) when no spectral adjustment, a linear spectral adjustment (used in the official HLS product), and the best modeled adjustment (following last section's conclusions) are applied using Sentinel 2A as a reference. The purple line represents the specified uncertainty based on the theoretical error budget of the Collection 5 MODIS [34]. The distribution of each band can also be seen through the histogram plotted on the left axis.

For the green band, the MR1 model overestimates the effect of the spectral adjustment, increasing the accuracy value from 0.001 to 0.0026. The red band, however, shows a significant improvement in the average accuracy of 54.6% with respect to using no spectral correction, with a similar average uncertainty and precision values. In the case of the NIR band, because the spectral responses of both sensors are almost identical, there is no discernible difference between the different methods and the APU values remain the same. Finally, the NDVI's accuracy is also improved by 62.5%, driven by the red band's improvement, maintaining a similar precision but increasing the uncertainty from 0.0267 to 0.0254 ($\sim 5\%$). The linear correction, on the other hand, improves the green band's average accuracy by 15%, but decreases its average accuracy by 25% in the red band and by 41% in the NDVI value.

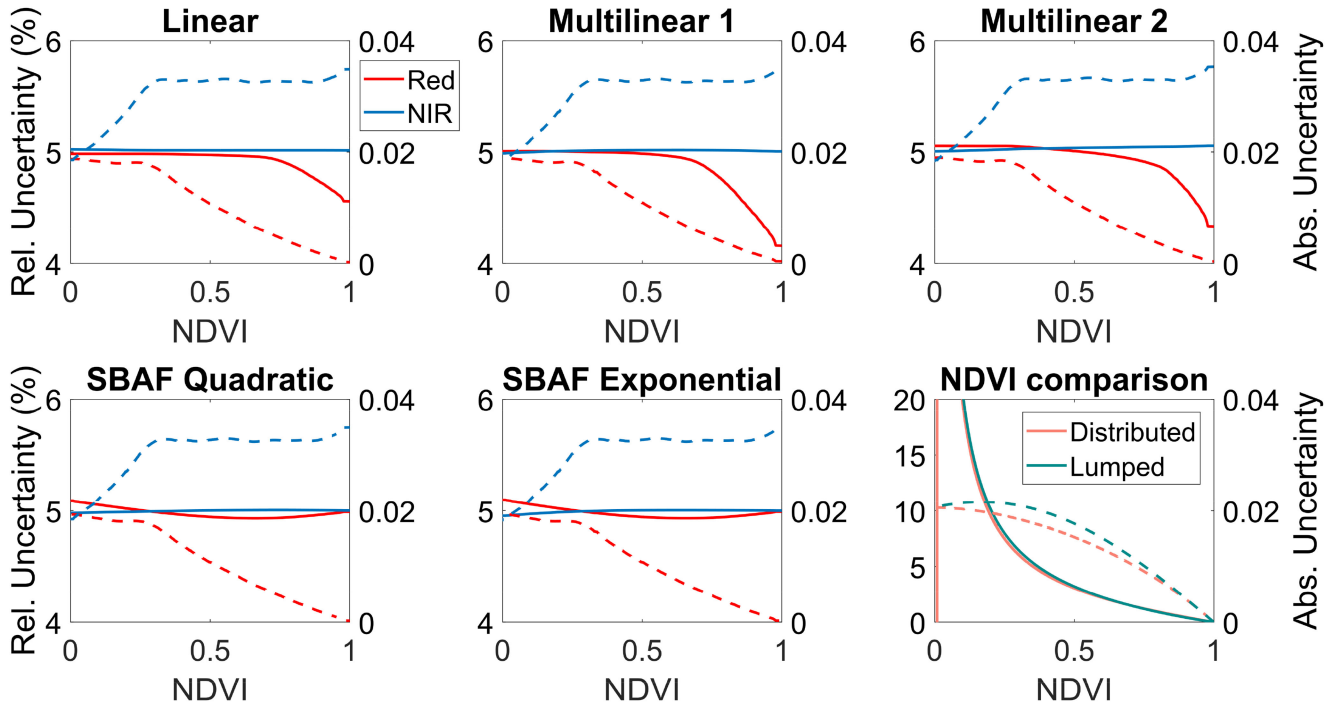


Fig. 5. First five graphs show the propagated relative (solid line–left axis) and absolute (dashed line–right axis) uncertainties for the different models applied as a function of the NDVI. The red and blue lines represent the values for the red and NIR bands, respectively. The bottom right graph compares the propagated relative and absolute errors for the distributed (red) and lumped (blue) methods. These results were modeled using MODIS Aqua as a reference and Landsat 8 as a target sensor, as an example.

D. AVHRR Time Series

Fig. 7 shows the difference between the NDVI trends computed using no spectral adjustment and using the MR1-Exp correction method as a function of the NDVI. The full 445 BEL-MANIP Site pixels containing different land surface types are considered. The results show how the difference is almost zero for $\text{NDVI} < 0.2$, but increases linearly with the NDVI, reaching discrepancies of ~ 0.05 for high NDVI values. The error bars for the difference have been propagated from the individual bars following (10).

V. DISCUSSION

A. Model Comparisons With Simulated Data

The reasoning behind these land cover dependencies is investigated in the sensitivity analysis performed in [19], which showed that the green peak region at 550 nm along with the red-NIR transitional region (680–780 nm) are the key factors in producing nonlinear patterns; spectral bands which are wide enough to cover these spectral regions will exhibit nonlinear land cover dependencies. The red band is the only band, which could have a wide enough RSR to cover both regions (see Fig. 1).

The results in Tables II and III confirmed our hypothesis that the models that provide the best cross-calibration performance differ between different bands, depending on how much and how many of these critical regions they cover. These results provide evidence that the green band's spectral bandpass differences also exhibit land cover dependencies as shown in the literature

for the red and NIR bands [4], [19], [20]. In the green band, the MR1 method was shown to be the best method in terms of precision and uncertainty, but not so much in the accuracy. The poor performance of the MR2 method in this band is due to two different factors. In the first place, the combination of the green-NIR bands to characterize land cover dependencies is not as strong as the red-NIR combination, despite the high correlation between the red-green bands. In the second place, the MR2 method is more likely to perform better when the LAI values are high and the NDVI saturates. In the case of the green band, the RSR functions are rarely wide enough to allow this to happen. For the NIR band, however, when the NDVI dependencies are very high due to a large band width, as is the case of NOAA14 compared to MODIS/Aqua, the MR2 characterized the land cover dependencies better by using the interaction terms between the red and NIR bands instead of the NDVI. This is evidenced with the better performance of the MR2 in accuracy, precision, and uncertainty.

In the red band, the SBAF exponential approach provides the best improvement of APU values, suggesting that not only is it preferred to the SBAF quadratic method when the RSR differences are high, but also when they are of similar value. When these differences are small, the simplicity and linearity of the three parameters provided by the SBAF quadratic method is recommended. When correcting the NDVI values, we found that, just like Fan and Liu 2017 [18], the distributed scheme yielded better results. Among the distributed scheme, we found that the best way to correct the NDVI value is to use the MR1 corrected NIR band and the SBAF exponential corrected red

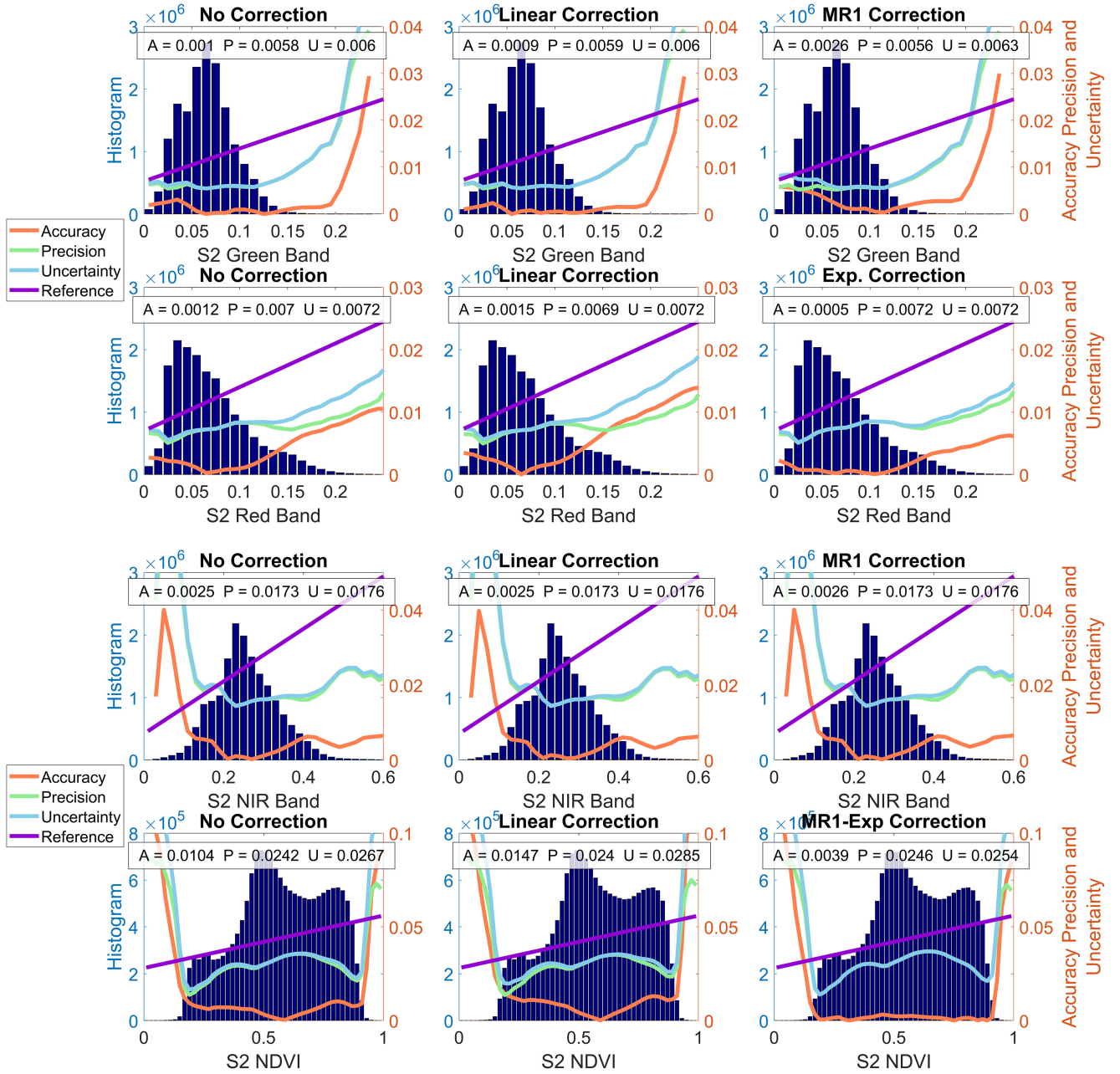


Fig. 6. Left axis shows the histogram of the green, red, NIR bands, and NDVI values. The right axis shows the accuracy (orange), precision (green), and uncertainty (blue) (APU). The purple line represents the specified uncertainty based on the theoretical error budget of the Collection 5 MODIS [34].

band, as opposed to using NIR and red bands corrected using the same model.

B. Propagation of Uncertainties

The small discrepancy in the relative and absolute errors between the different models indicates that the choice of the correction equation does not introduce significant errors in the spectral adjustment. We can safely select the best method in terms of the theoretical performance through the APU values. Independent of the magnitude of the uncertainty differences, the adjustment significantly increases the accuracy of the data. This bias cannot be accounted for with the uncertainty propagation.

When analyzing the NDVI computation, the small differences between the lumped and distributed methods point to a similar conclusion; there is not a preferable way to compute the NDVI in terms of uncertainty propagation. Given that the distributed method provides a better improvement in APU values with respect to the modeled data, it is still chosen as the preferable option.

C. HLS Product

The discrepancies between the data and the model observed in the green band are likely due to the small spectral adjustment discrepancies ($\sim 1.5\%$) and the presence of other sources of error

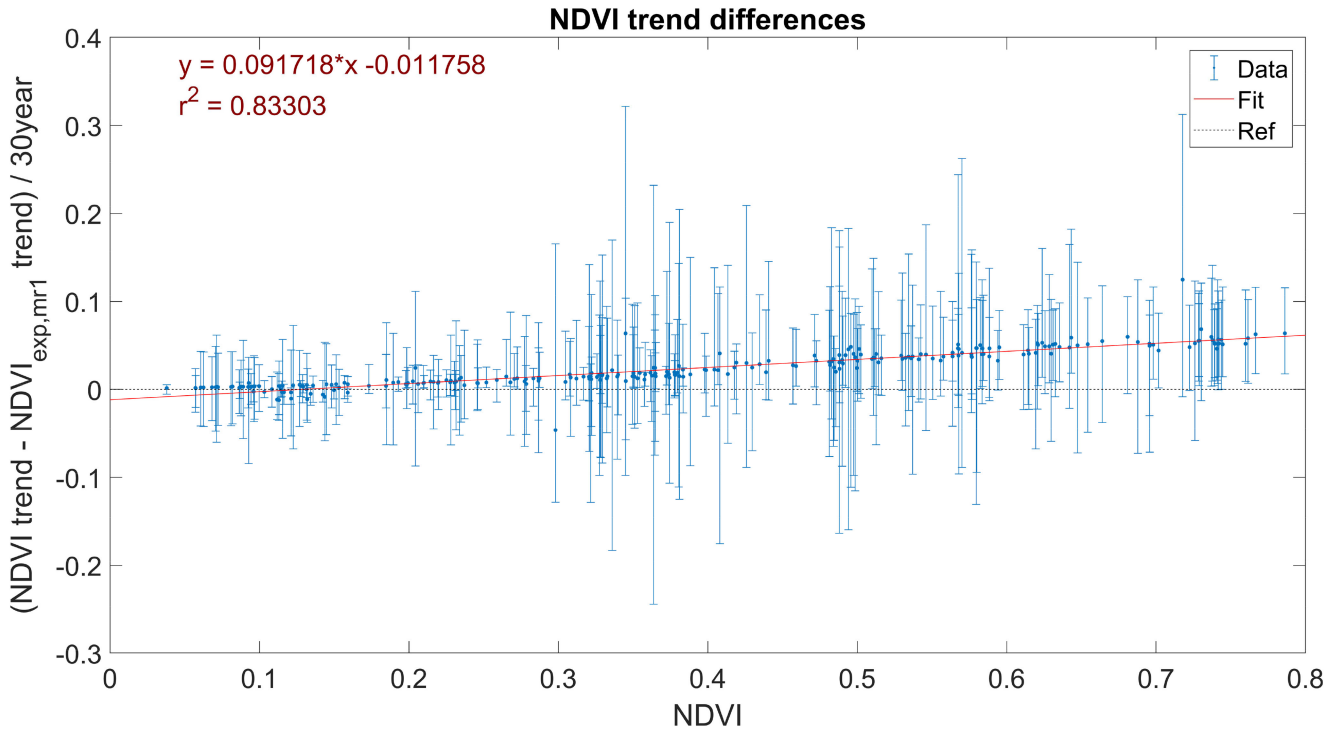


Fig. 7. NDVI trends difference between using no spectral adjustment correction and using the MR1-Exp correction as a function of the NDVI for 445 BELMANIP2 site pixels. The red solid and black dotted lines represent the least squares fit and the reference, respectively.

of the same order. Comparing the spectral differences between two satellites with similar RSR functions is always a difficult task, given the small contribution it has on the disagreement between the data compared to other sources of error. In this case, we selected view zenith angles close to nadir observation to minimize the effects due to the surface's anisotropy, but because we were working with surface reflectance, errors due to sensor calibration, atmospheric correction, and pixel misregistration could appear. From these errors, the sensor calibration has a performance of better than 3% [41], and atmospheric correction after sensor calibration propagation has uncertainties of $\sim 7\%$ and $\sim 4\%$ in the green and red bands, respectively. These values are higher than the spectral adjustment differences ($\sim 1.5\%$ and $\sim 3\%$) [10], [42]. For this reason, the discrepancies between the data and the model observed in the green band for this study are expected. The unbiased NIR band indicates that errors due to misregistration are negligible, because L8 and S2 NIR RSRs are almost identical. In the case of the red band and NDVI, the results in Fig. 6 show that the use of a model that accounts for land cover dependencies like the SBAF exponential, increases the accuracy of the product by 54.6% and 62.5%, respectively.

D. AVHRR Time Series

The results in Fig. 7 show that the trends of NDVI values pixels are sensitive to the spectral adjustment method used and could even change from being positive to negative outside of the error margin when the NDVI value is high. For low NDVI values, however, the difference is negligible. This is expected, given that the differences between the reference and target sensor increase

with the NDVI. Overall, the trends are overestimated, especially for NDVI values higher than 0.4, when land cover dependencies start becoming evident. In the case of the red and NIR bands, not shown in this paper, the trends were underestimated for the red band and overestimated for the NIR band, especially when the NDVI value is high. These results highlight the importance of an accurate spectral adjustment when computing long-term trends of the NDVI and surface reflectance data.

VI. CONCLUSION

Obtaining spectral coefficients which can be applied to global data requires a large spatial and temporal distribution of measurements, which only satellite data can provide. As long as other sources of error are comparable to the spectral adjustment differences, this becomes a difficult task. Until then we must rely on models that can simulate satellite data, and our approach of linearly combining field measurements addresses this. The regression parameters retrieved are operationally convenient and provide a significant correction of the spectral effects for coarse to moderate resolution satellite sensors. These results benefit existing cross-correlation methods by allowing a smoother transition between different sensor generations and facilitating the use of a time series using data from multiple satellites.

ACKNOWLEDGMENT

The authors would like to thank the anonymous reviewers whose useful suggestions significantly increased the quality of this paper.

REFERENCES

- [1] G. Chander *et al.*, "Applications of spectral band adjustment factors (SBAF) for cross-calibration," *IEEE Trans. Geosci. Remote Sens.*, vol. 51, no. 3, pp. 1267–1281, Mar. 2013.
- [2] P. M. Teillet, G. Fedosejevs, K. Thome, and J. L. Barker, "Impacts of spectral band difference effects on radiometric cross-calibration between satellite sensors in the solar-reflective spectral domain," *Remote Sens. Environ.*, vol. 110, no. 3, pp. 393–409, Oct. 2007.
- [3] J. Franke, V. Heinzl, and G. Menz, "Assessment of NDVI- differences caused by sensor specific relative spectral response functions," in *Proc. IEEE Int. Symp. Geosci. Remote Sens.*, 2006, pp. 1138–1141.
- [4] A. P. Trishchenko, J. Cihlar, and Z. Li, "Effects of spectral response function on surface reflectance and NDVI measured with moderate resolution satellite sensors," *Remote Sens. Environ.*, vol. 81, no. 1, pp. 1–18, Jul. 2002.
- [5] P. Teillet, J. Barker, B. Markham, R. Irish, G. Fedosejevs, and J. Storey, "Radiometric cross-calibration of the Landsat-7 ETM+ and Landsat-5 TM sensors based on tandem data sets," *Remote Sens. Environ.*, vol. 78, no. 1/2, pp. 39–54, Oct. 2001.
- [6] M. Dinguirard and P. N. Slater, "Calibration of space-multispectral imaging sensors: A review," *Remote Sens. Environ.*, vol. 68, no. 3, pp. 194–205, Jun. 1999.
- [7] S. Skakun, C. O. Justice, E. Vermote, and J.-C. Roger, "Transitioning from MODIS to VIIRS: An analysis of inter-consistency of NDVI data sets for agricultural monitoring," *Int. J. Remote Sens.*, vol. 39, no. 4, pp. 971–992, Feb. 2018.
- [8] M. Drusch *et al.*, "Sentinel-2: ESA's optical high-resolution mission for GMES operational services," *Remote Sens. Environ.*, vol. 120, pp. 25–36, May 2012.
- [9] J. Li and D. P. Roy, "A global analysis of Sentinel-2A, Sentinel-2B and Landsat-8 data revisit intervals and implications for terrestrial monitoring," *Remote Sens.*, vol. 9, no. 9, Aug. 2017, Art. no. 902.
- [10] M. Claverie *et al.*, "The harmonized landsat and Sentinel-2 data set," *Remote Sens. Environ. Rev.*, vol. 219, pp. 145–161, 2018.
- [11] X. Fan and Y. Liu, "A generalized model for intersensor NDVI calibration and its comparison with regression approaches," *IEEE Trans. Geosci. Remote Sens.*, vol. 55, no. 3, pp. 1842–1852, Mar. 2017.
- [12] Y. Kim, A. R. Huete, T. Miura, and Z. Jiang, "Spectral compatibility of vegetation indices across sensors: Band decomposition analysis with Hyperion data," *J. Appl. Remote Sens.*, vol. 4, no. 1, Mar. 2010, Art. no. 043520.
- [13] M. D. Steven, T. J. Malthus, F. Baret, H. Xu, and M. J. Chopping, "Inter-calibration of vegetation indices from different sensor systems," *Remote Sens. Environ.*, vol. 88, no. 4, pp. 412–422, Dec. 2003.
- [14] P. S. Thenkabail, "Inter-sensor relationships between IKONOS and Landsat-7 ETM+ NDVI data in three ecoregions of Africa," *Int. J. Remote Sens.*, vol. 25, no. 2, pp. 389–408, Jan. 2004.
- [15] C. Martínez-Beltrán, M. A. O. Jochum, A. Calera, and J. Meliá, "Multi-sensor comparison of NDVI for a semi-arid environment in Spain," *Int. J. Remote Sens.*, vol. 30, no. 5, pp. 1355–1384, Mar. 2009.
- [16] W. J. D. van Leeuwen, B. J. Orr, S. E. Marsh, and S. M. Herrmann, "Multi-sensor NDVI data continuity: Uncertainties and implications for vegetation monitoring applications," *Remote Sens. Environ.*, vol. 100, no. 1, pp. 67–81, Jan. 2006.
- [17] M. Claverie, J. Masek, and J. Ju, "Harmonized Landsat-8 Sentinel-2 (HLS) Product User's Guide," Product Version 1.4, 2016.
- [18] X. Fan and Y. Liu, "A comparison of NDVI intercalibration methods," *Int. J. Remote Sens.*, vol. 38, no. 19, pp. 5273–5290, Oct. 2017.
- [19] T. Miura, A. Huete, and H. Yoshioka, "An empirical investigation of cross-sensor relationships of NDVI and red/near-infrared reflectance using EO-1 Hyperion data," *Remote Sens. Environ.*, vol. 100, no. 2, pp. 223–236, Jan. 2006.
- [20] X. Fan and Y. Liu, "A global study of NDVI difference among moderate-resolution satellite sensors," *ISPRS J. Photogramm. Remote Sens.*, vol. 121, pp. 177–191, Nov. 2016.
- [21] P. D'Odorico, A. Gonsamo, A. Damm, and M. E. Schaepman, "Experimental evaluation of Sentinel-2 spectral response functions for NDVI time-series continuity," *IEEE Trans. Geosci. Remote Sens.*, vol. 51, no. 3, pp. 1336–1348, Mar. 2013.
- [22] C. O. Justice *et al.*, "An overview of MODIS Land data processing and product status," *Remote Sens. Environ.*, vol. 83, no. 1, pp. 3–15, Nov. 2002.
- [23] X. Xiong, J. Sun, X. Xie, W. L. Barnes, and V. V. Salomonson, "On-orbit calibration and performance of aqua MODIS reflective solar bands," *IEEE Trans. Geosci. Remote Sens.*, vol. 48, no. 1, pp. 535–546, Jan. 2010.
- [24] S. Liang *et al.*, "Validating MODIS land surface reflectance and albedo products: Methods and preliminary results," *Remote Sens. Environ.*, vol. 83, no. 1, pp. 149–162, Nov. 2002.
- [25] Z. Wan, "New refinements and validation of the MODIS land-surface temperature/emissivity products," *Remote Sens. Environ.*, vol. 112, no. 1, pp. 59–74, Jan. 2008.
- [26] N. US Department of Commerce, "ESRL global monitoring division - GRAD - Surface radiation budget network (SURFRAD)," [Online]. Available: <https://www.esrl.noaa.gov/gmd/grad/surfrad/sitepage.html>. Accessed: Jun. 27, 2018.
- [27] D. P. Roy, J. Li, H. K. Zhang, L. Yan, H. Huang, and Z. Li, "Examination of Sentinel-2A multi-spectral instrument (MSI) reflectance anisotropy and the suitability of a general method to normalize MSI reflectance to nadir BRDF adjusted reflectance," *Remote Sens. Environ.*, vol. 199, pp. 25–38, Sep. 2017.
- [28] B. Franch, E. Vermote, J.-C. Roger, I. Becker-Reshef, and C. O. Justice, "A 30+ year AVHRR land surface reflectance climate 2 data record and its application to wheat yield 3 monitoring," *Remote Sens.*, vol. 9, 2016, Art. no. 296.
- [29] E. Vermote, C. O. Justice, and F. M. Breon, "Towards a generalized approach for correction of the BRDF effect in MODIS directional reflectances," *IEEE Trans. Geosci. Remote Sens.*, vol. 47, no. 3, pp. 898–908, Mar. 2009.
- [30] B. Franch, E. F. Vermote, J. A. Sobrino, and Y. Julien, "Retrieval of surface Albedo on a daily basis: Application to MODIS data," *IEEE Trans. Geosci. Remote Sens.*, vol. 52, no. 12, pp. 7549–7558, Dec. 2014.
- [31] F. Baret *et al.*, "Evaluation of the representativeness of networks of sites for the global validation and intercomparison of land biophysical products: Proposition of the CEOS-BELMANIP," *IEEE Trans. Geosci. Remote Sens.*, vol. 44, no. 7, pp. 1794–1803, Jul. 2006.
- [32] R. F. Kokaly, D. G. Despain, R. N. Clark, and K. E. Livo, "Mapping vegetation in Yellowstone National Park using spectral feature analysis of AVIRIS data," *Remote Sens. Environ.*, vol. 84, no. 3, pp. 437–456, Mar. 2003.
- [33] R. F. Kokaly *et al.*, "USGS Spectral Library Version 7," U.S. Geological Survey, Reston, VA, USA, USGS Numbered Series 1035, 2017.
- [34] E. F. Vermote and S. Kotchenova, "Atmospheric correction for the monitoring of land surfaces," *J. Geophys. Res. Atmos.*, vol. 113, no. D23, Dec. 2008, Art. no. D23S90.
- [35] J. M. Chen, "Spatial scaling of a remotely sensed surface parameter by contexture," *Remote Sens. Environ.*, vol. 69, no. 1, pp. 30–42, Jul. 1999.
- [36] D. Haboudane, J. R. Miller, E. Pattey, P. J. Zarco-Tejada, and I. B. Strachan, "Hyperspectral vegetation indices and novel algorithms for predicting green LAI of crop canopies: Modeling and validation in the context of precision agriculture," *Remote Sens. Environ.*, vol. 90, no. 3, pp. 337–352, Apr. 2004.
- [37] H. B. Mann, "Nonparametric tests against trend," *Econometrica*, vol. 13, no. 3, pp. 245–259, 1945.
- [38] M. Kendall and J. D. Gibbons, *Rank Correlation Methods*, 5th ed. London, U.K.: Oxford Univ. Press, 1990.
- [39] P. K. Sen, "Estimates of the regression coefficient based on Kendall's Tau," *J. Amer. Stat. Assoc.*, vol. 63, no. 324, pp. 1379–1389, Dec. 1968.
- [40] M. Hollander, D. A. Wolfe, and E. Chicken, *Nonparametric Statistical Methods*. Hoboken, NJ, USA: Wiley, 1973.
- [41] H. K. Zhang *et al.*, "Characterization of Sentinel-2A and Landsat-8 top of atmosphere, surface, and nadir BRDF adjusted reflectance and NDVI differences," *Remote Sens. Environ.*, vol. 215, pp. 482–494, Sep. 15, 2018.
- [42] E. Vermote, C. Justice, M. Claverie, and B. Franch, "Preliminary analysis of the performance of the Landsat 8/OLI land surface reflectance product," *Remote Sens. Environ.*, vol. 185, pp. 46–56, Nov. 2016.



Jose Luis Villares-Nadal received the Bachelor's degree in physics and the M.Sc. degree in remote sensing from the University of Valencia, Valencia, Spain, in 2015 and 2016, respectively. He is currently working toward the Ph.D. degree at the University of Maryland, College Park, MD, USA.

He is currently a Research Assistant with the NASA Goddard Space Flight Centre, Greenbelt, MD. His research interests include cross-calibration methods, BRDF correction and land surface albedo retrieval, specifically for global studies application using coarse spatial resolution sensors.



Belen Franch received the Ph.D. degree in physics from the University of Valencia, Valencia, Spain, in 2013.

She is currently a Research Assistant Professor with the Department of Geographical Sciences, University of Maryland, College Park, MD, USA, and a Science Collaborator in the NASA Goddard Space Flight Center. Her research interests include agriculture monitoring, atmospheric correction in the solar spectral range, the study and application of BRDF inversion methods, and land surface albedo estimation

and analysis. She provides research support for the EOFsAC and is a collaborator in the GEOGLAM Project. She is also a Professor on remote sensing with the University of Maryland, Department of Geographical Sciences.



Jean-Claude Roger received the Ph.D. degree in atmospheric physics from the University of Lille 1, Villeneuve-d'Ascq, France, in 1991 for a thesis on "Spatial Studies in Polarized Light - Preparation of the POLDER instrument."

He became a Full Professor in atmospheric physics with the University Blaise Pascal, Clermont-Ferrand, France, in 2007. He is currently a Research Professor with the Department of Geographical Sciences, University of Maryland, College Park, MD, USA.

He also works at the NASA Goddard Space Flight Center, code 619, Greenbelt, USA. He does research for land and atmosphere applications (remote sensing, radiative transfer, polarization, field experiments, etc.). He is particularly involved in atmospheric correction, aerosols characterization for climatic impact, land product with application to agriculture, satellite Cal/Val exercises, and Radiative transfer code development like 6S. He is Co-Pi of the CEOS-WGCV ACIX and CEOS-WGCV ACIX II - CMIX.



Eric F. Vermote received the Ph.D. degree in atmospheric optics from the University of Lille, Lille, France, in 1990.

Until 2012, he was a Research Professor with the Department of Geographical Sciences, University of Maryland, College Park, MD, USA. He is currently a Research Physical Scientist with the Terrestrial Information Systems Laboratory, NASA Goddard Space Flight Center, Greenbelt, MD. He is a member of the Moderate Resolution Imaging Spectroradiometer Science Team, the NASA National Polar orbiting

Operational Environmental Satellite System Preparatory Project Science Team for the Visible Infrared Imaging Radiometer Suite Instrument, and the Landsat Data Continuity Mission Science Team and is responsible for the atmospheric correction over land surfaces in the visible to middle infrared. His research interests include radiative transfer modeling, vicarious calibration, atmospheric correction, aerosol retrieval, and the generation of climate data record for terrestrial studies.



Sergii Skakun received the M.S. (Hons.) degree in applied mathematics from the Physics and Technology Institute, NTUU "Kyiv Polytechnic Institute," Kyiv, Ukraine, in 2004, and the Ph.D. degree in computer science from the National Academy of Sciences of Ukraine, Kiev, Ukraine, in 2005.

He is currently an Associate Research Professor with the Department of Geographical Sciences, University of Maryland, College Park, MD, USA, and a Research Scientist with the Terrestrial Information Systems Laboratory, NASA Goddard Space Flight

Center, Greenbelt, MD, USA. His research interests include advancing methods, models and emerging technologies in the area of data science for heterogeneous remote sensing data fusion, processing and analysis, and their applications to the areas of societal benefit.



Chris Justice received the Ph.D. degree from the University of Reading, Reading, U.K., in 1977.

He became a Professor and the Research Director of Geography with the University of Maryland, in 2001 and in 2010, became the Department Chair to the Department of Geographical Sciences. He is a Program Scientist for NASA's Land Cover Land Use Change Program. He is the Land Discipline Leader for the NASA Moderate Imaging Spectroradiometer (MODIS) and the Soumi-NPP VIIRS Science Team and is responsible for the MODIS Fire Product. He

is the Co-Chair of the NASA LANCE User Working Group. He is a member of the international GOC/GOLD-Fire Implementation Team. He is the Co-Chair of the GEOGLAM Initiative. His current research is on land cover and land use change, land observations and data products, global agricultural monitoring, and their associated information technology and decision support systems.